# Large Sensitivity of Near-Surface Vertical Vorticity Development to Heat Sink Location in Idealized Simulations of Supercell-Like Storms

PAUL M. MARKOWSKI AND YVETTE P. RICHARDSON

*Department of Meteorology, The Pennsylvania State University, University Park, Pennsylvania*

(Manuscript received 23 December 2016, in final form 26 February 2017)

ABSTRACT

In idealized numerical simulations of supercell-like ''pseudostorms'' generated by a heat source and sink in a vertically sheared environment, a tornado-like vortex develops if air possessing large circulation about a vertical axis at the lowest model levels can be converged. This is most likely to happen if the circulation-rich air possesses only weak negative buoyancy (the circulation-rich air has a history of descent, so typically possesses at least some negative buoyancy) and is subjected to an upward-directed vertical perturbation pressure gradient force. This paper further explores the sensitivity of the development of near-surface vertical vorticity to the horizontal position of the heat sink. Shifting the position of the heat sink by only 2–3 km can significantly influence vortex intensity by altering both the baroclinic generation of circulation and the buoyancy of circulation-rich air. Many of the changes in the pseudostorms that arise from shifting the position of the heat sink would be difficult to anticipate. The sensitivity of the pseudostorms to heat sink position probably at least partly explains the well-known sensitivity of near-surface vertical vorticity development to the microphysics parameterizations in more realistic supercell storm simulations, as well as some of the failures of actual supercells to produce tornadoes in seemingly favorable environments.

## 1. Introduction

Markowski and Richardson (2014, hereafter MR14) showed that a simple numerical model consisting of only a heat source and sink in an environment containing streamwise horizontal vorticity can reproduce many aspects of the supercell thunderstorms observed in nature. The heat source drives an updraft that rotates cyclonically owing to the upward tilting of the streamwise horizontal vorticity imposed in the environment. The heat sink, centered northeast of the heat source, drives a downdraft that mimics the precipitation-driven downdraft of an actual storm.

Within an airstream that passes through the heat sink en route to the updraft, significant cyclonic vorticity is acquired at the lowest model levels owing to the enhanced upward tilting of near-surface horizontal vorticity that is possible within an airstream that previously has descended. The horizontal vorticity within the descending airstream is enhanced by both baroclinic vorticity generation (attributable to the horizontal temperature gradients associated with the heat sink) and horizontal vorticity stretching (mass continuity implies horizontal accelerations of air parcels within the descending airstream; streamwise accelerations can greatly intensify the streamwise vorticity) (Rotunno et al. 2017). Cyclonic vorticity also can develop while air is still descending owing to the effect described by Davies-Jones and Brooks (1993) and Davies-Jones (2000), whereby the combination of baroclinity and descent causes the vorticity vector to be inclined upward relative to the velocity vector (this is sometimes referred to as the ''DJB effect''; Dahl et al. 2014). In summary, at the lowest model levels, large cyclonic vorticity tends to be confined to regions comprising air parcels that previously have descended, which also tend to be regions of negative buoyancy given the parcels' prior histories within the heat sink.

In the MR14 simulations, a tornado-like vortex develops at the lowest model level if circulation-rich, near-surface air is associated with weak negative buoyancy and also experiences a large upward-directed vertical perturbation pressure gradient force (VPPGF) owing to its proximity to the overlying heat source and associated midlevel updraft and mesocyclone. This is most likely to happen when the heat sink is of intermediate strength and the environmental low-level shear is strong.

*Corresponding author e-mail*: Dr. Paul Markowski, pmarkowski@psu.edu

DOI: 10.1175/JAS-D-16-0372.1

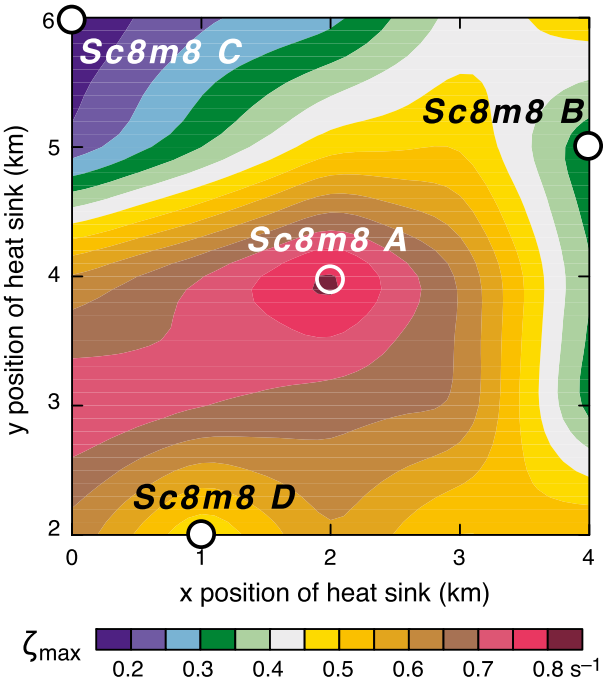


FIG. 1. Magnitude of the cyclonic vorticity maximum $\zeta_{max}$ as a function of the horizontal position of the heat sink relative to the heat source in MR14's Sc8m8 simulations. The $x$ and $y$ axes indicate the heat sink coordinates ($x_c$, $y_c$) (km), which are each shifted up to ±2 km from the location of the heat sink in the default MR14 Sc8m8 simulation (referred to as Sc8m8 A; the Sc8m8 A heat sink position is indicated with the open white circle). The positions of the heat sink in simulations Sc8m8 B, C, and D are indicated with the filled white circles. Adapted from MR14's Fig. 24a, which is derived from 25 simulations (all have the same resolution as the default Sc8m8 simulation in MR14).

However, as noted in MR14, vortex development also is sensitive to the horizontal position of the heat sink (Fig. 1). One could interpret the sensitivity as implying that outflow from a heat sink having weak negative buoyancy and being subjected to a strong upward VPPGF at low levels are necessary but insufficient conditions for the development of intense near-surface cyclonic vorticity. In actual supercells, outflow having weak negative buoyancy (a storm trait often associated with environments having high boundary layer relative humidity; Markowski et al. 2002; Shabbott and Markowski 2006) and the presence of a strong, upward-directed VPPGF at low levels (an updraft trait associated with strong low-level vertical shear in the environment; MR14) are insufficient conditions for tornadogenesis as well, given that not all supercells in environments known to be supportive of these favorable storm attributes produce tornadoes.

In this article, we further explore the sensitivity of vortex development in the MR14 simulations to the location of the heat sink. Section 2 reviews the MR14 methodology and describes the additional numerical experiments performed herein. The findings are presented in section 3. Some discussion and concluding remarks are presented in section 4.

## 2. Methodology

As in MR14, the dry version of Cloud Model, version 1 (CM1; Bryan and Fritsch 2002), release 16, is used. The domain is 100 km × 100 km × 18 km, with rigid, free-slip top and bottom boundaries, and open lateral boundaries. The horizontal grid spacing is 100 m within a 20 km × 20 km region centered in the domain and gradually increases to 3.9 km from the edge of this inner region to the lateral boundaries. The vertical grid spacing varies from 100 m in the lowest 1 km to 400 m at the top of the domain. The large (small) time step is 1.0 s (0.1 s). An updraft is driven by a cylindrical heat source extending from $z$ = 500 m to 10 km, having a radius of 3 km; its maximum intensity is at $z$ = 5.25 km. The updraft rotates cyclonically at midlevels owing to the vertically sheared environment in which winds turn clockwise with height. However, vertical vorticity does not develop at the lowest levels until cool air emanating from a cylindrical heat sink, which is activated 900 s into the simulations, underspreads the updraft. The heat sink also has a radius of 3 km, but it is centered north or northeast of the heat source (to be explained below), spans the lowest 5 km, and has its maximum strength at the surface. Additional details pertaining to the simulation design are explained in MR14. Even though the MR14 simulations contain no moist processes, the simulations are potentially revealing about the sensitivity of tornadogenesis to subtleties in the shape and location of the cold pool and, by implication, microphysical processes. In an actual supercell, the location, size, and amplitude of the "heat sink" (i.e., the distribution of latent cooling) is affected by the deep-layer wind shear, storm-relative winds, hydrometeor fall speeds, and hydrometeor species.

The focus of this paper is on variations of MR14's Sc8m8 simulation (see their Figs. 5–13), in which a tornado-like vortex develops, attaining a maximum vertical vorticity ($\zeta_{max}$) of 0.83 s$^{-1}$ at $t$ = 2760 s (Fig. 2a). The simulation features strong environmental low-level shear and a moderately strong heat sink centered 4 km north and 2 km east of the heat source (the heat sink amplitude is $S_{c0} = -0.008$ K s$^{-1}$ and the low-level shear parameter is $m$ = 8, using the symbology of MR14). Herein, this simulation is referred to as Sc8m8 A, which is compared to three other simulations—Sc8m8 B, C, and D—in which the heat sink's position relative to the heat source is varied and leads to considerably lesser

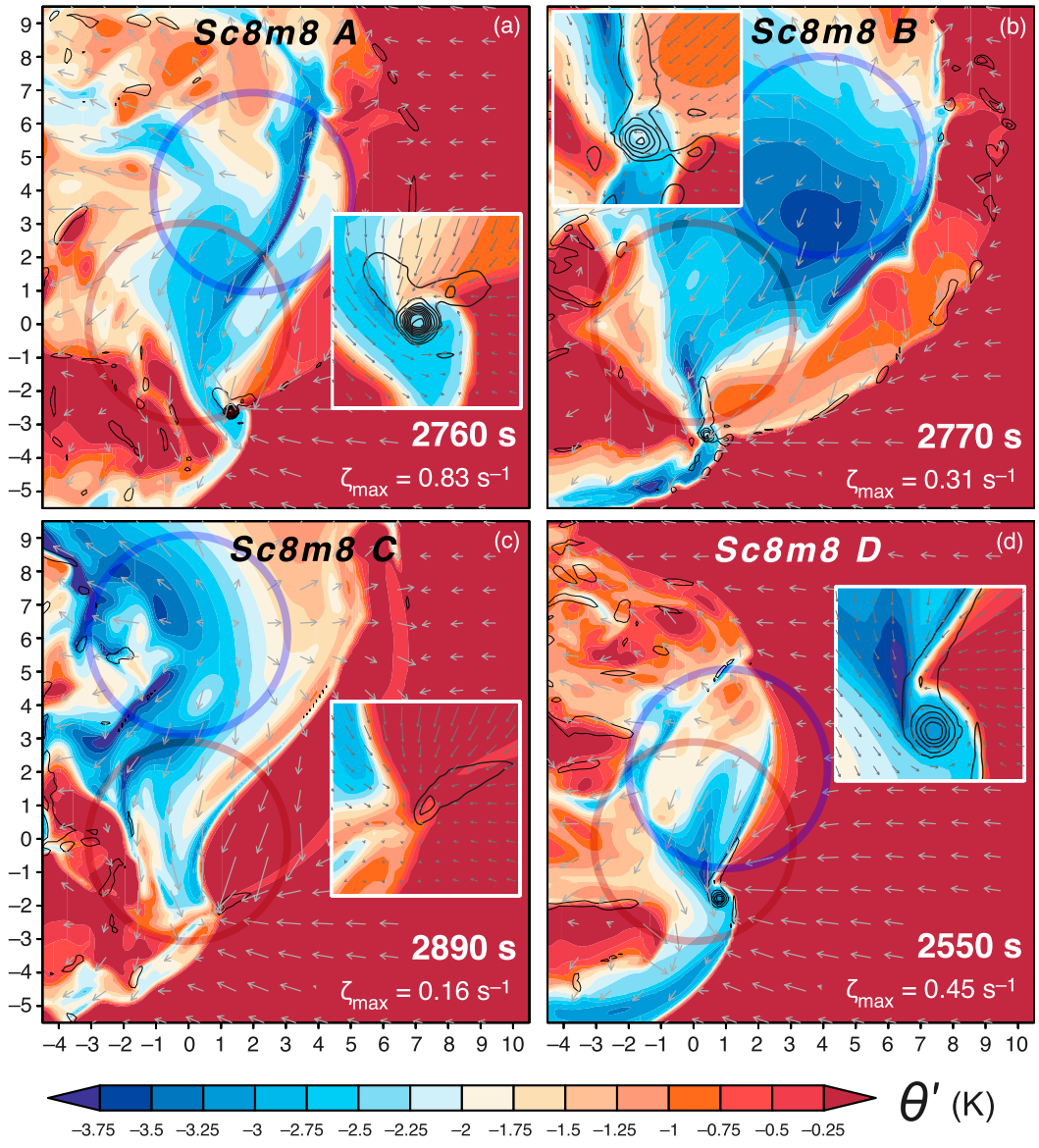


FIG. 2. Horizontal cross sections of potential temperature perturbation ($\theta'$; color) at $z = 50$ m at the time of $\zeta_{max}$ in the Sc8m8 (a) A, (b) B, (c) C, and (d) D simulations. Wind vectors depict storm-relative winds and black contours are $\zeta = 0.01, 0.05, 0.10, 0.15, 0.20, \ldots$ s$^{-1}$. The times and values of $\zeta_{max}$ are indicated in each panel, as are the horizontal projections of the heat source and sink (light red and light blue rings, respectively). Axis labels are in kilometers. Insets show zoomed-in views centered on $\zeta_{max}$.

$\zeta_{max}$ (Fig. 1). In simulation Sc8m8 B, the heat sink is centered 1 km north and 2 km east of the heat sink position in simulation Sc8m8 A; $\zeta_{max}$ of 0.31 s$^{-1}$ is reached 2770 s into the simulation (Fig. 2b). In simulation Sc8m8 C, the heat sink is centered 2 km north and 2 km west of the default heat sink position; $\zeta_{max}$ of 0.16 s$^{-1}$ is reached at 2890 s (Fig. 2c). In simulation Sc8m8 D, the heat sink is centered 2 km south and 1 km west of the default heat sink position; $\zeta_{max}$ of 0.45 s$^{-1}$ is reached at 2550 s (Fig. 2d).

The strength of the low-level, upward-directed VPPGF and magnitude of the negative buoyancy acquired by parcels that pass through the heat sink are relatively easily controlled in the model by the environmental low-level vertical shear and heat sink amplitude (which are identical in simulations Sc8m8 A–D), respectively. However, the development of near-surface circulation and the potential collocation of circulation-rich air with a strong upward-directed VPPGF are extremely sensitive to the details of the buoyancy field, its

gradients, and parcel trajectories, all of which are sensitive to the location of the heat sink, as well as its three-dimensional structure, though the latter is not investigated here.

## 3. Results

Three possible explanations to be explored for the weaker vortex formation in simulations Sc8m8 B, C, and D (relative to Sc8m8 A) are (i) the development of less near-surface circulation; (ii) the development of similar near-surface circulation, but with the circulation-rich air being too far removed from where the upward-directed VPPGF is strong (it tends to be maximized near the heat source); and (iii) the development of similar near-surface circulation, and in a favorable location relative to the heat source, but with the circulation-rich air being too negatively buoyant. With respect to (iii), even though the heat sink amplitude is identical in all of the experiments, it is possible for the buoyancy of the circulation-rich air to differ owing to changes in parcel trajectories and residence times within the heat sink, among other factors, brought about by changing the position of the heat sink.

The near-surface potential temperature perturbation ($\theta'$) fields among the four simulations have some obvious differences at the times that $\zeta_{max}$ is obtained (Fig. 2), though it is not obvious to us that the differences in the $\theta'$ fields would lead to the $\zeta_{max}$ differences. The cold pool in experiment Sc8m8 B (Fig. 2b) is larger and stronger than the cold pools in the other experiments, and the cold pool in the Sc8m8 D experiment (Fig. 2d) is the smallest and weakest.[1] Much of the variation in cold pool size and strength can be attributed to the degree of "overlap" in the regions spanned by the heat source and heat sink (the horizontal projections of the heat source and sink are indicated in Fig. 2). Within regions of overlap, both the heat source and heat sink are weakened. This overlap also influences the strength of the low-level drafts. For example, the weakest low-level updraft is in simulation D (Fig. 3d), and the low-level updrafts are strongest in simulations B and C (Figs. 3b,c). Though the cold pool and updraft differences complicate the comparisons between the simulations, this situation might not differ much from actual storms; for example, sometimes a heavy precipitation shaft (which contributes to negative buoyancy) is partially located within updraft as opposed to being completely separated from the updraft. The updraft would be weakened, but evaporative cooling within the precipitation shaft would also be limited given that the precipitation would be falling through a saturated column of air.

Figure 4 displays the near-surface circulation $C$ computed about 1-km-radius rings centered on each grid point, where $C = \oint \mathbf{v} \cdot \mathbf{dl}$, $\mathbf{v}$ is the velocity, and $\mathbf{dl}$ is a vector line element of the rings about which $C$ is computed. The cyclonic vortices that develop within simulations Sc8m8 A and D are associated with the largest $C$ ($>4 \times 10^4\,m^2\,s^{-1}$). Simulations B and C have considerably less $C$ ($\sim 2.2 \times 10^4$ and $\sim 1.2 \times 10^4\,m^2\,s^{-1}$, respectively). In all four simulations, the circulation-rich air has at least some overlap with the low-level updraft and significant upward-directed, dynamic VPPGF (Fig. 3), unlike the intense vortexgenesis "failure modes" reported in MR14 when the heat sink was strong or the low-level environmental vertical wind shear was weak. In those cases, the circulation-rich air was displaced several kilometers to the south of the strongest upward-directed VPPGF (e.g., the Sc16m8 and Sc8m2 simulations in MR14; see Figs. 16a and 19a, respectively, in MR14).

As in MR14, material circuits also are tracked backward in time from the 1-km-radius rings that are centered on $\zeta_{max}$ in each simulation (Fig. 5). The material circuits reveal the dynamical reasons for the circulation differences [see MR14 and Markowski (2016) for further information]. The rings are introduced at $z = 150$ m (i.e., one vertical grid length above the first interior grid level) rather than at $z = 50$ m, which is the altitude at which $C$ is displayed in Fig. 4. Doing so yields more accurate circulation budget calculations (Fig. 6b), presumably owing to the fact that fewer parcels comprising the circuits drop below the first interior grid point, at which point winds and circulation forcings must be extrapolated to the parcels. The rings initially contain 10 000 parcels (i.e., many more than are shown in Fig. 5), and parcels are added to the rings as necessary in order to ensure that the distance between adjacent parcels does not exceed 20 m as the trajectories are stepped backward in time. Errors in the line integral calculations required for the computation of $C$ and its forcings become unacceptably large if the folds and bends, which unavoidably develop within the material circuits as they are tracked backward in time, are not well resolved. The trajectory calculations use velocity data that have been saved every 5 s.

[1] References to cold pool strength as strong versus weak refer to the magnitude of the negative buoyancy at the lowest grid level. At the request of a reviewer, the Rotunno et al. (1988) cold pool parameter, $[-2g\int_0^H(\theta'/\overline{\theta})\,dz]^{1/2}$, where $H$ is the cold pool depth and $g$ is the gravitational acceleration, also was computed (not shown). The correlations between the cold pool parameter and $\theta'$ at the lowest grid level range from $-0.93$ to $-0.84$ at the time of maximum cyclonic vorticity in the four simulations.

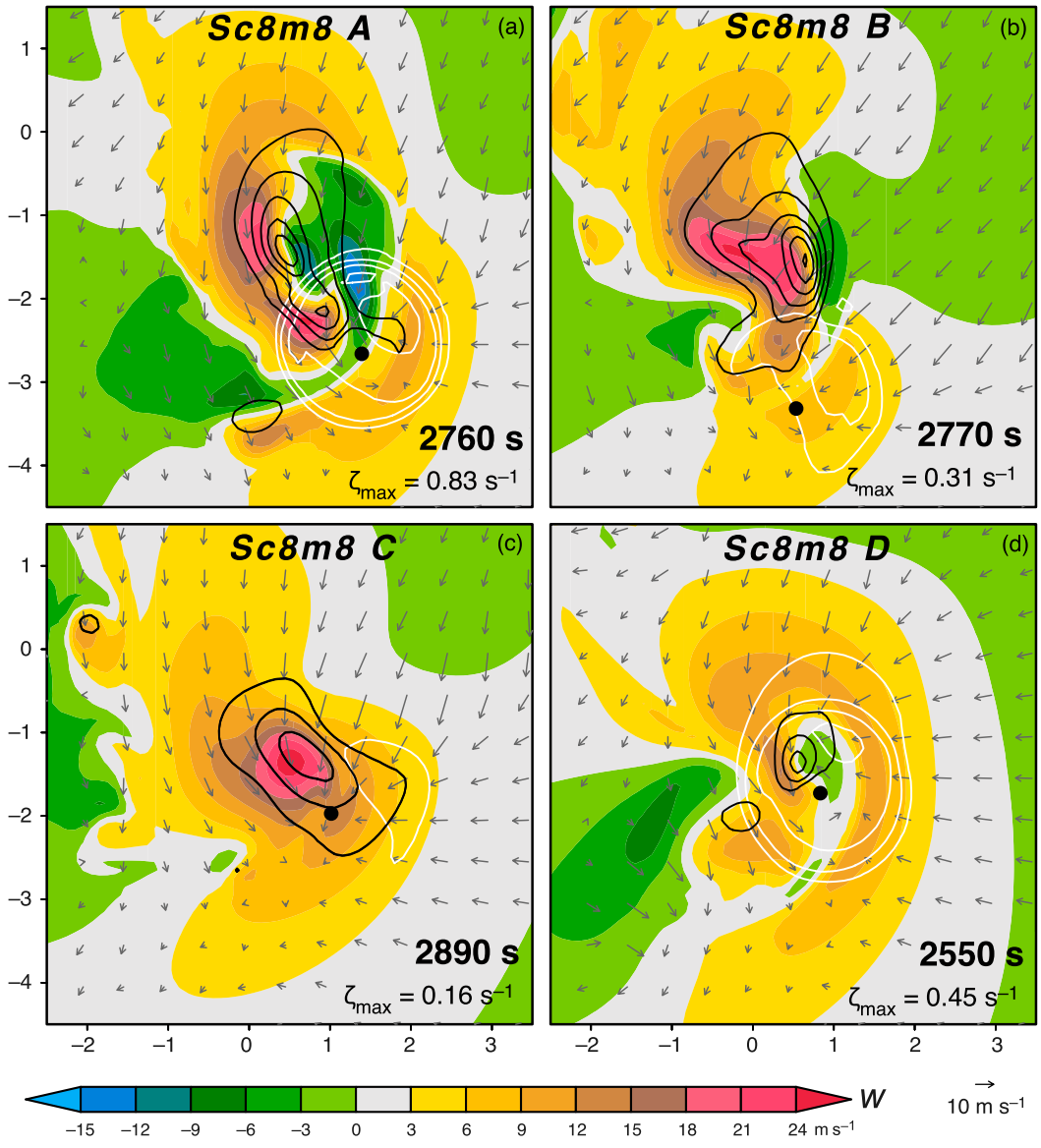


FIG. 3. Horizontal cross sections of vertical velocity ($w$; color) at $z = 1.05$ km at the time of $\zeta_{max}$ in the Sc8m8 (a) A, (b) B, (c) C, and (d) D simulations (the region shown is smaller than the region shown in Figs. 2, 4, 5, and 7). Wind vectors depict storm-relative winds at $z = 50$ m. White contours are circulation (see also Fig. 4) at $z = 50$ m, contoured every $10 \times 10^4$ m$^2$ s$^{-1}$ starting at $10 \times 10^4$ m$^2$ s$^{-1}$. Black contours are mean dynamic vertical perturbation pressure gradient acceleration in the lowest 1.05 km, contoured every 0.1 m s$^{-2}$ starting at 0.1 m s$^{-2}$. The black dots indicate the locations of the $\zeta$ maxima. The times and values of $\zeta_{max}$ are indicated in each panel. Axis labels are in kilometers.

In simulations Sc8m8 A and D, baroclinically generated circulation ($C^{BC} = \int\oint B\,dz\,dt$, where $B = g\theta'/\overline{\theta}$ is the buoyancy, and $\overline{\theta}$ is the environmental potential temperature) is large (Fig. 6b) and dominates the total $C$ (Fig. 6a). Although simulation Sc8m8 D has an overall weaker cold pool than Sc8m8 A, $C^{BC}$ is actually larger in simulation Sc8m8 D than in Sc8m8 A [the total $C$ is similar in the two simulations because of larger negative contributions in simulation Sc8m8 D from turbulent and numerical diffusion (not shown)]. The horizontal $\theta'$ gradient in simulation Sc8m8 D immediately upstream (north) of the cyclonic vortex area is stronger than in Sc8m8 A despite the overall weaker cold pool in Sc8m8 D. Moreover, the circulation-rich air is closer to the heat source and associated dynamic upward forcing in simulation Sc8m8 D than in Sc8m8 A, which one might suspect would be more favorable for intense vortex

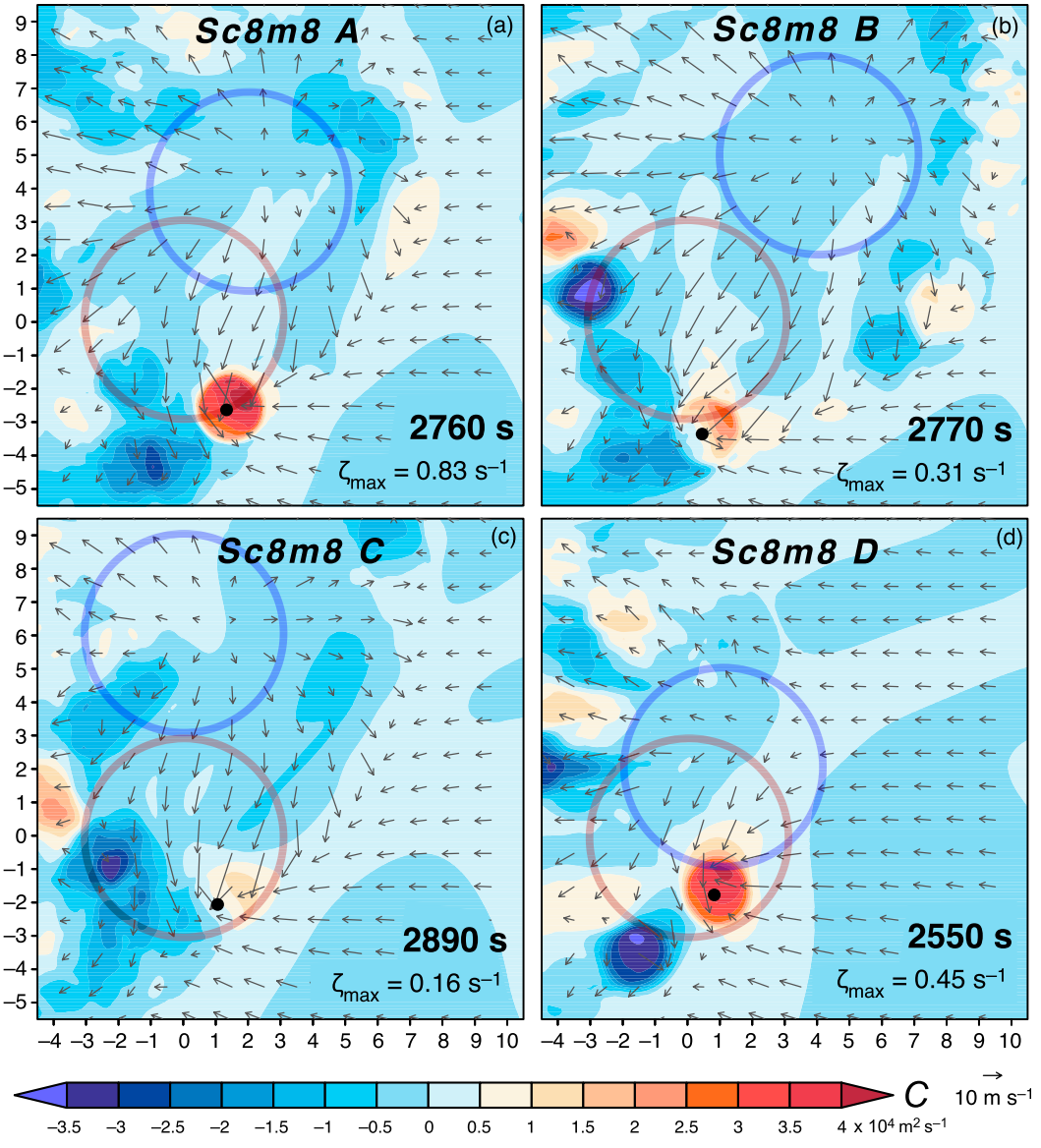


FIG. 4. As in Fig. 2, but for circulation $C$ computed around 1-km-radius rings centered on each grid point. The black dots indicate the locations of the $\zeta$ maxima.

development. However, the circulation-rich air is associated with greater negative buoyancy in simulation Sc8m8 D than in Sc8m8 A. Of the possible reasons enumerated at the beginning of this section for why a vortex would be weaker, it appears as though the vorticity maximum in simulation Sc8m8 D is weaker for reason (iii). That is, sufficient $C$ develops, and circulation-rich air is favorably located with respect to the upward-directed VPPGF that tends to be maximized at low levels near the heat source (cf. Figs. 3a,d); however, the circulation-rich air is more negatively buoyant in simulation Sc8m8 D than in Sc8m8 A (cf. Figs. 2a,d). We believe that it would have been virtually impossible to anticipate this given that the Sc8m8 D cold pool is actually weaker overall than the cold pool in Sc8m8 A.

Considerably less $C^{BC}$ develops about the material circuits that converge upon the near-surface cyclonic vorticity maxima in simulations Sc8m8 B and C (Fig. 6b). Surprisingly, $C^{BC}$ is actually *negative* for both of these material circuits. In simulation Sc8m8 B, the total $C$ about the circuit decreases in time as the circuit approaches $\zeta_{max}$ (Fig. 6a). This circuit has a larger $C$ in the far field (i.e., at $t = 600$ s) than the material circuits tracked in the other simulations. In simulation Sc8m8 C, the circuit (slightly) gains $C$ during its approach toward $\zeta_{max}$ despite the development of negative $C^{BC}$,

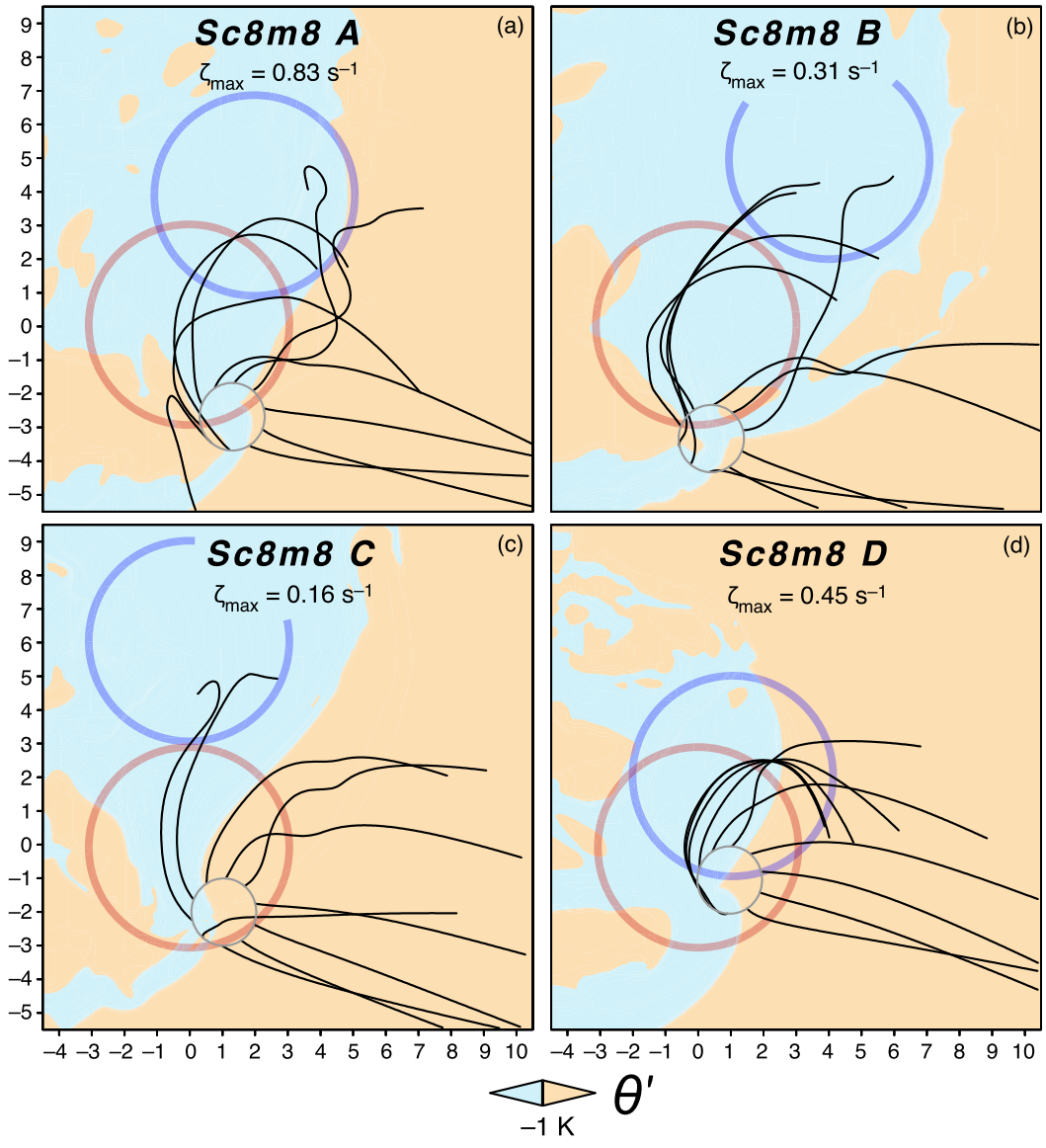


FIG. 5. Horizontal projections of backward trajectories, 10 min in duration, originating at the time of $\zeta_{max}$, from 10 equally spaced points along the 1-km-radius rings centered on $\zeta_{max}$ at $z = 150$ m in the Sc8m8 (a) A, (b) B, (c) C, and (d) D simulations. The region within which $\theta' < -1$ K is shaded blue.

owing to positive contributions from turbulent and numerical diffusion (not shown). Referring to the opening paragraph of this section, it appears as though the vorticity maxima in simulations Sc8m8 B and C are weaker for reason (i)—that is, lesser *C*. In comparing the trajectories of simulations Sc8m8 A and D and Sc8m8 B and C (Fig. 5), it is not obvious that the modified heat sink positions would lead to such profound differences in the development of circulation at the lowest model levels.

Last, given the possibility, afforded by storm chasers' mobile phones, of routinely available meso-$\gamma$-scale pressure observations within storms in the near future (Mass and Madaus 2014), we also explored whether systematic differences exist between the pressure fields of simulation Sc8m8 A and simulations Sc8m8 B, C, and D. Unfortunately, though there are obvious differences in the pressure fields of the simulations (Fig. 7), it is not obvious to us that these differences would be associated with the differences in vortex intensity that have been noted. The heat sinks are associated with high pressure anomalies proportional in strength to the strength of the cold pools. Low pressure is present between the cyclonic vortices and the high pressure regions associated with

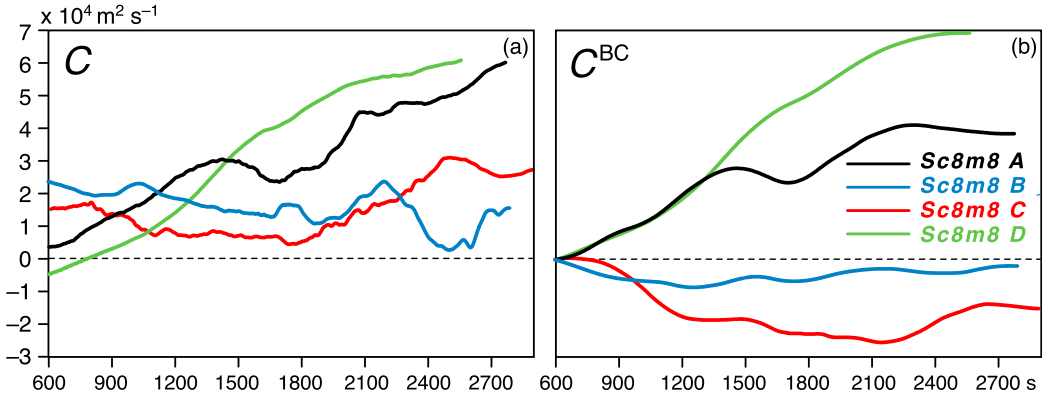


FIG. 6. (a) Circulation ($C$) and (b) baroclinic circulation ($C^{BC}$) about material circuits followed backward in time to 600 s from the time of $\zeta_{max}$ in the Sc8m8 A, B, C, and D simulations.

the heat sinks. These low pressure regions have the same dynamical origins as the "inflow lows" explained by Davies-Jones (2002).

## 4. Discussion and concluding remarks

The results presented above demonstrate how relatively small changes in only the horizontal position of the heat sink—less than the horizontal grid spacing of today's operational convection-allowing models—can lead to substantial changes in the pseudostorms, including the development of near-surface cyclonic vorticity. The sensitivity of the pseudostorms to heat sink position probably at least partly explains the well-known sensitivity of near-surface vertical vorticity development to the microphysics parameterizations of more realistic supercell storm simulations (e.g., Gilmore et al. 2004; Snook and Xue 2008; Dawson et al. 2010, 2015). Many of the changes in the pseudostorms would be virtually impossible to anticipate, such as how shifting the heat sink approximately 2 km east-northeast from its position in simulation Sc8m8 A to the position in simulation Sc8m8 B would yield such large differences in the baroclinic generation of circulation (large positive versus small negative $C^{BC}$ per Fig. 6b). The differences in the pressure fields, temperature fields, and trajectories are often subtle, and even when they are not so subtle, it is not obvious that these fields will be associated with the development of inferior vertical vortices.

It seems likely that near-surface vortex development within real supercells would be at least as sensitive to the characteristics of the precipitation field as in the "pseudostorms" in the highly idealized MR14 simulations. Given the relative simplicity of the MR14 simulations, it might not be surprising to find that actual supercells exhibit even greater sensitivity. Moreover, it seems reasonable to assume that variations in heat sink geometry (i.e., not just location) also would expose large sensitivities.

Although the development of near-surface cyclonic vortices is sensitive to the horizontal position of the heat sink, it is not possible to generalize exactly how the shifting of the heat sink away from its optimal position in simulation Sc8m8 A leads to weaker vortices. In two cases (Sc8m8 B and C), considerably less circulation is generated, and in a third case (Sc8m8 D), circulation is comparable to that which develops in the default simulation (Sc8m8 A), but the circulation-rich air is more negatively buoyant, which reduces upward accelerations and vorticity stretching. In the small sample of simulations herein, no evidence of a "failure mode" involving the development of large circulation, but in an unfavorable location (i.e., far from a region of dynamically forced upward accelerations), was identified; such a failure mode was identified in MR14 for a stronger heat sink.

The sensitivity of the pseudostorms to heat sink position probably also explains some of the failures of actual supercells to produce tornadoes in seemingly favorable environments. Nationwide, the tornado warning false-alarm rate remains high (~75%–80%), despite the fact that forecasters generally are limiting warning issuance to environments known to be favorable for tornadoes (Anderson-Frey et al. 2016). One must conclude that many environments seem very supportive of tornadoes based on known ingredients [e.g., convective available potential energy, vertical wind shear (with especially large shear in the lower troposphere), and high boundary layer relative humidity (e.g., Thompson et al. 2003)], yet fail to yield tornadoes. Yet on some rare days (e.g., the tornado outbreaks on 3 May 1999 in central Oklahoma and 27 April 2011 in the southeastern

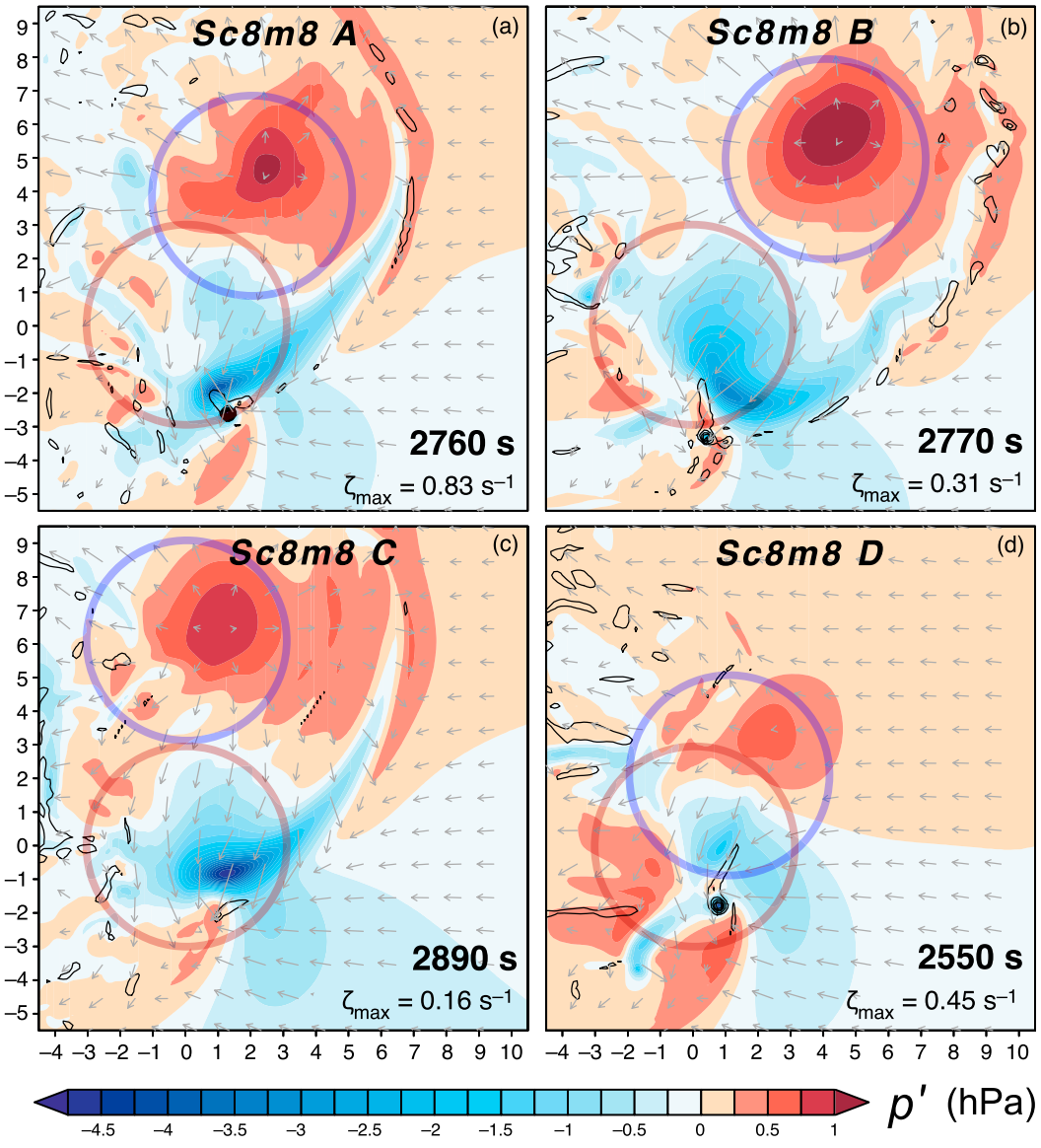


FIG. 7. As in Fig. 2, but for pressure perturbation ($p'$).

United States), nearly every storm is tornadic. What is special about these days? Do the storms on these days somehow *all* have optimal cold pool strengths and shapes (i.e., heat sink characteristics)? This would seem to be extremely unlikely. Or is there something about some environments—yet to be discovered—that can make storms much less sensitive to the details of their cold pools?

*Acknowledgments.* We thank the anonymous reviewers for their critical evaluations of this work. We also thank George Bryan for the use of his numerical model and for his many years of support. This work would not have been possible without the generous support of the National Science Foundation (Grants AGS-1157646 and AGS-1536460).

## REFERENCES

Anderson-Frey, A. K., Y. P. Richardson, A. R. Dean, R. L. Thompson, and B. T. Smith, 2016: Investigation of near-storm environments for tornado events and warnings. *Wea. Forecasting*, **31**, 1771–1790, doi:10.1175/WAF-D-16-0046.1.

Bryan, G. H., and J. M. Fritsch, 2002: A benchmark simulation for moist nonhydrostatic numerical models. *Mon. Wea. Rev.*, **130**, 2917–2928, doi:10.1175/1520-0493(2002)130<2917:ABSFMN>2.0.CO;2.

Dahl, J. M. L., M. D. Parker, and L. J. Wicker, 2014: Imported and storm-generated near-ground vertical vorticity in a

simulated supercell. *J. Atmos. Sci.*, **71**, 3027–3051, doi:10.1175/JAS-D-13-0123.1.

Davies-Jones, R., 2000: A Lagrangian model for baroclinic genesis of mesoscale vortices. Part I: Theory. *J. Atmos. Sci.*, **57**, 715–736, doi:10.1175/1520-0469(2000)057<0715:ALMFBG>2.0.CO;2.

——, 2002: Linear and nonlinear propagation of supercell storms. *J. Atmos. Sci.*, **59**, 3178–3205, doi:10.1175/1520-0469(2003)059<3178:LANPOS>2.0.CO;2.

——, and H. E. Brooks, 1993: Mesocyclogenesis from a theoretical perspective. *The Tornado: Its Structure, Dynamics, Prediction, and Hazards*, *Geophys. Monogr.*, Vol. 79, Amer. Geophys. Union, 105–114, doi:10.1029/GM079p0105.

Dawson, D. T., M. Xue, J. A. Milbrandt, and M. K. Yau, 2010: Comparison of evaporation and cold pool development between single-moment and multimoment bulk microphysics schemes in idealized simulations of tornadic thunderstorms. *Mon. Wea. Rev.*, **138**, 1152–1171, doi:10.1175/2009MWR2956.1.

——, ——, ——, and A. Shapiro, 2015: Sensitivity of real-data simulations of the 3 May 1999 Oklahoma City tornadic supercell and associated tornadoes to multimoment microphysics. Part I: Storm- and tornado-scale numerical forecasts. *Mon. Wea. Rev.*, **143**, 2241–2265, doi:10.1175/MWR-D-14-00279.1.

Gilmore, M. S., J. M. Straka, and E. N. Rasmussen, 2004: Precipitation and evolution sensitivity in simulated deep convective storms: Comparisons between liquid-only and simple ice and liquid phase microphysics. *Mon. Wea. Rev.*, **132**, 1897–1916, doi:10.1175/1520-0493(2004)132<1897:PAESIS>2.0.CO;2.

Markowski, P. M., 2016: An idealized numerical simulation investigation of the effects of surface drag on the development of near-surface vertical vorticity in supercell thunderstorms. *J. Atmos. Sci.*, **73**, 4349–4385, doi:10.1175/JAS-D-16-0150.1.

——, and Y. P. Richardson, 2014: The influence of environmental low-level shear and cold pools on tornadogenesis: Insights from idealized simulations. *J. Atmos. Sci.*, **71**, 243–275, doi:10.1175/JAS-D-13-0159.1.

——, J. M. Straka, and E. N. Rasmussen, 2002: Direct surface thermodynamic observations within the rear-flank downdrafts of nontornadic and tornadic supercells. *Mon. Wea. Rev.*, **130**, 1692–1721, doi:10.1175/1520-0493(2002)130<1692:DSTOWT>2.0.CO;2.

Mass, C. F., and L. E. Madaus, 2014: Surface pressure observations from smartphones: A potential revolution for high-resolution weather prediction? *Bull. Amer. Meteor. Soc.*, **95**, 1343–1349, doi:10.1175/BAMS-D-13-00188.1.

Rotunno, R., J. B. Klemp, and M. L. Weisman, 1988: A theory for strong, long-lived squall lines. *J. Atmos. Sci.*, **45**, 463–485, doi:10.1175/1520-0469(1988)045<0463:ATFSLL>2.0.CO;2.

——, P. M. Markowski, and G. H. Bryan, 2017: ''Near-ground'' vertical vorticity in supercell thunderstorm models. *J. Atmos. Sci.*, doi:10.1175/JAS-D-16-0288.1, in press.

Shabbott, C. J., and P. M. Markowski, 2006: Surface in situ observations within the outflow of forward-flank downdrafts of supercell thunderstorms. *Mon. Wea. Rev.*, **134**, 1422–1441, doi:10.1175/MWR3131.1.

Snook, N., and M. Xue, 2008: Effects of microphysical drop size distribution on tornadogenesis in supercell thunderstorms. *Geophys. Res. Lett.*, **35**, L24803, doi:10.1029/2008GL035866.

Thompson, R., R. Edwards, J. Hart, K. Elmore, and P. Markowski, 2003: Close proximity soundings within supercell environments obtained from the Rapid Update Cycle. *Wea. Forecasting*, **18**, 1243–1261, doi:10.1175/1520-0434(2003)018<1243:CPSWSE>2.0.CO;2.